https://doi.org/10.5194/egusphere-2024-684
Preprint. Discussion started: 26 March 2024

3D Geo-Modeling Framework for Multisource Heterogeneous Data Fusion Based on Multimodal Deep Learning and Multipoint Statistics: A case study in South China Sea

Hengguang Liu[1], Shaohong Xia[1*], Chaoyan Fan[1], Changrong Zhang[1]

1. Key Laboratory of Ocean and Marginal Sea Geology, South China Sea Institute of Oceanology, Chinese Academy of Sciences, Guangzhou 510301, China

Corresponding author: Shaohong Xia (shxia@scsio.ac.cn)

Abstract

Relying on geological data to construct 3D models can provide a more intuitive and easily comprehensible spatial perspective. This process aids in exploring underground spatial structures and geological evolutionary processes, providing essential data and assistance for the exploration of geological resources, energy development, engineering decision-making, and various other applications. As one of the methods for 3D geological modeling, multipoint statistics can effectively describe and reconstruct the intricate geometric shapes of nonlinear geological bodies. However, existing multipoint statistics algorithms still face challenges in efficiently extracting and reconstructing the global spatial distribution characteristics of geological objects. Moreover, they lack a data-driven modeling framework that integrates diverse sources of heterogeneous data. This research introduces a novel approach that combines multipoint statistics with multimodal deep artificial neural networks and constructs the 3D crustal P-wave velocity structure model of the South China Sea by using 44 OBS forward profiles, gravity anomalies, magnetic anomalies and topographic relief data. The experimental results demonstrate that the new approach surpasses multipoint statistics and Kriging interpolation methods, and can generate a more accurate 3D geological model through the integration of multiple geophysical data. Furthermore, the reliability of the 3D crustal P-wave velocity

https://doi.org/10.5194/egusphere-2024-684
Preprint. Discussion started: 26 March 2024

structure model, established using the novel method, was corroborated through visual and statistical analyses. This model intuitively delineates the spatial distribution characteristics of the crustal velocity structure in the South China Sea, thereby offering a foundational data basis for researchers to gain a more comprehensive understanding of the geological evolution process within this region.

Keywords: multipoint statistics, multimodal deep learning, South China Sea, 3D crustal velocity structure model

1.Introduction

3D modeling of the geological bodies and structures can be realized based on geological data such as boreholes and profiles, providing more intuitive and easier-to-understand descriptions. Therefore, the construction of 3D geological models has become an important analytical tool for studying the formation and evolution of the Earth. It not only provides a foundation and framework for various geological applications such as spatial analysis (Lindsay et al., 2012), energy exploration (Yin et al., 2011), resource prediction (Kaufmann et al., 2008; Ma et al., 2018), and engineering construction (Qu et al., 2015; Zhang et al., 2019), but also offers a multi-perspective understanding of geological objects from a microscopic scale, such as micrometer to centimeter scale (Song et al., 2018; Li et al., 2019).

The MultiPoint Statistics (MPS) method, a technique for 3D modeling, leverages the correlation features between multiple points in space derived from a training image (TI). This is achieved by incorporating conditional data and prior geological knowledge during the simulation process. The MPS approach effectively addresses the limitations of two-point statistics, such as the Kriging interpolation algorithm, in measuring spatial correlation of data. It provides an effective description and reconstruction of the complex geometric shapes of nonlinear geological bodies (Mariethoz et al., 2010).

However, limited by the method of extracting spatial patterns from TI, most MPS

https://doi.org/10.5194/egusphere-2024-684
Preprint. Discussion started: 26 March 2024

methods cannot consider the global spatial structure characteristics of the modeled objects in the reconstruction process (Hou et al., 2023). Moreover, in order to construct a more reliable 3D geologic model, it is necessary to integrate data obtained from various observation methods for modeling, thereby reducing the ambiguity caused by modeling based on a single source of data. Existing MPS algorithms lack an integrated framework for handling multi-source heterogeneous data. Directly using multiple heterogeneous data sources as soft data constraints makes it difficult to apply them directly to the simulation process, ignoring the physical significance of the data. This approach also fails to capture the coupling and differences between the data, and the selection of their weights is relatively subjective (Hansen et al., 2018; Wang et al., 2022; Yin et al., 2011).

One of the solutions for 3D simulation based on multi-source heterogeneous data in the field of MPS is to integrate a data fusion framework by incorporating multimodal deep learning techniques. In such a framework , multiple geophysical data can be integrated, which makes it possible to extract feature distributions and coupling relationships between different geophysical data, thereby improving modeling accuracy. At the same time, the ability of deep learning to extract and reconstruct features from datasets (Hou et al., 2023; Chen et al., 2020; Cui et al., 2022) can be used to comprehensively consider the global spatial characteristics of various geological objects during the modeling process.

Drawing upon the aforementioned concepts, our study developed a 3D geological modeling algorithm that amalgamates multimodal deep learning with MPS. We applied this algorithm to the South China Sea (SCS) as a representative case study. The SCS is not only a crucial strategic zone for China in terms of energy, economy, and security but also an important frontier region for studying continental rifting, seafloor spreading processes, and deep-seated dynamic mechanisms. The SCS is one of the largest marginal basins in the western Pacific Ocean, situated at the intersection of the Eurasian Plate, the Indian-Australian Plate, and the Pacific Plate. It formed during the Oligocene-Middle Miocene (33-15 Ma) through seafloor spreading (Li et al., 2014; Taylor and Hayes, 1983; Piao et al., 2022). Its evolution has been influenced by the interaction of continental and oceanic plates, making it one of the most active zones of tectonic movement globally (Liu, 2011; Xia et al., 2018; Xie et al., 2022). Complex tectonic processes such as continental collision and subduction, have shaped the present-day tectonic patterns in the SCS, making it a natural laboratory for studying continental rifting, seafloor spreading processes, and deep-seated dynamic mechanisms. Additionally, the SCS is also one of the most important offshore areas for oil and gas reserves, as well as natural gas hydrates in China (Wu et al., 2005; Wang et al., 2011; Xu et al., 2022). These resources have significant strategic value, and their exploration is an important aspect of China's deep-sea strategy. Therefore, constructing a 3D crustal P-wave velocity structure model of the SCS can provide important data foundation for studying its tectonic evolution, resource exploration, and other related research.

Currently, there exists no comprehensive and publicly accessible 3D crustal P-wave velocity structure model of the SCS, which impedes research in Earth sciences and interdisciplinary studies. Additionally, due to natural topographical conditions and constraints in manpower and resources, large-scale data exploration is challenging. The methods employed often depend on point sources or line sources, leading to a paucity of data relative to the study area. Furthermore, various exploration methods yield different types of geological data such as borehole data, profile data, mineral geological data, and hydrogeological data. These data have distinct organizational forms and distribution ranges, complicating their effective integration for geological understanding.

In this study, we integrate deep learning method, geostatistical method, and multi-source heterogeneous data fusion techniques to investigate the theory and methods of stochastic modeling of 3D geological structures. The new method overcomes the limitations of traditional algorithms in characterizing non-stationary geological structures under conditions of single or sparse data, providing new approaches for constructing large-scale and high-precision 3D geological models. In addition, high-resolution forward profiles and multi-source geophysical data were collected and used to construct a 3D crustal P-wave velocity structure model of the

https://doi.org/10.5194/egusphere-2024-684
Preprint. Discussion started: 26 March 2024

SCS, which can support the study of tectonic evolution, dynamic mechanisms, resource exploration, and related issues in SCS.

This paper is structured into six sections: the first introduces the current state of research and existing issues with 3D stochastic modeling methods; the second outlines the data foundation employed in this study; the third presents proposed methods; the fourth features modeling examples based on the forward velocity structure profiles of the SCS; the fifth examines and discusses the performance of the algorithms applied to these examples; and the final section provides a comprehensive summary.

2.Data Foundation

The seismic exploration data and geological information accumulated in the SCS have diverse characteristics, making it challenging to directly incorporate data from different sources, scales, dimensions, and storage formats into the construction of a 3D model. To effectively utilize these geological data, several steps must be taken. First, it is essential to standardize the representation and storage formats of the data, converting similar types of data into consistent graphical or textual formats. Second, the standardization of units and coding methods for similar data types ensures accurate retrieval and matching with clear numerical standards. Finally, unifying the spatiotemporal framework of different data categories and establishing a consistent spatial coordinate system allows for the establishment of spatial relationships between different types of data. This enables the construction of a heterogeneous database at different scales.

After data sorting, the modeling process in this study divides the data into two parts: the target modeling data and the auxiliary data. The former includes the attributes of the 3D geological information model that needs to be constructed, which is related to spatial coordinates (X, Y, Z). In this study, the target modeling data are used as MPS TIs, deep learning label data, and constraints for the modeling

https://doi.org/10.5194/egusphere-2024-684
Preprint. Discussion started: 26 March 2024

process. The latter corresponds to attributes that are not part of the 3D modeling objectives and covers the study area in a 2D plane, which is related to spatial coordinates (X, Y). This type of data can serve as input data for the deep learning framework of fusing multi-source heterogeneous data. Some of this auxiliary data directly related to the distribution of some geological attributes in the 3D geological model will constrain the modeling process, such as DEM data and geological maps. In this study, the target modeling data used are forward modeling of P-wave velocity structure in two-dimensional profile form.

In this study, the velocity structure profiles are used as the target modeling data. 44 forward-simulated velocity structure profiles, with OBS as the main detection instrument, were collected from different locations in the SCS (Table 1). The distribution of these profiles in the SCS is shown in Fig. 1. After redrawing these forward profiles by tracing and unifying color labels, the colors were converted to grayscale values.

https://doi.org/10.5194/egusphere-2024-684
Preprint. Discussion started: 26 March 2024

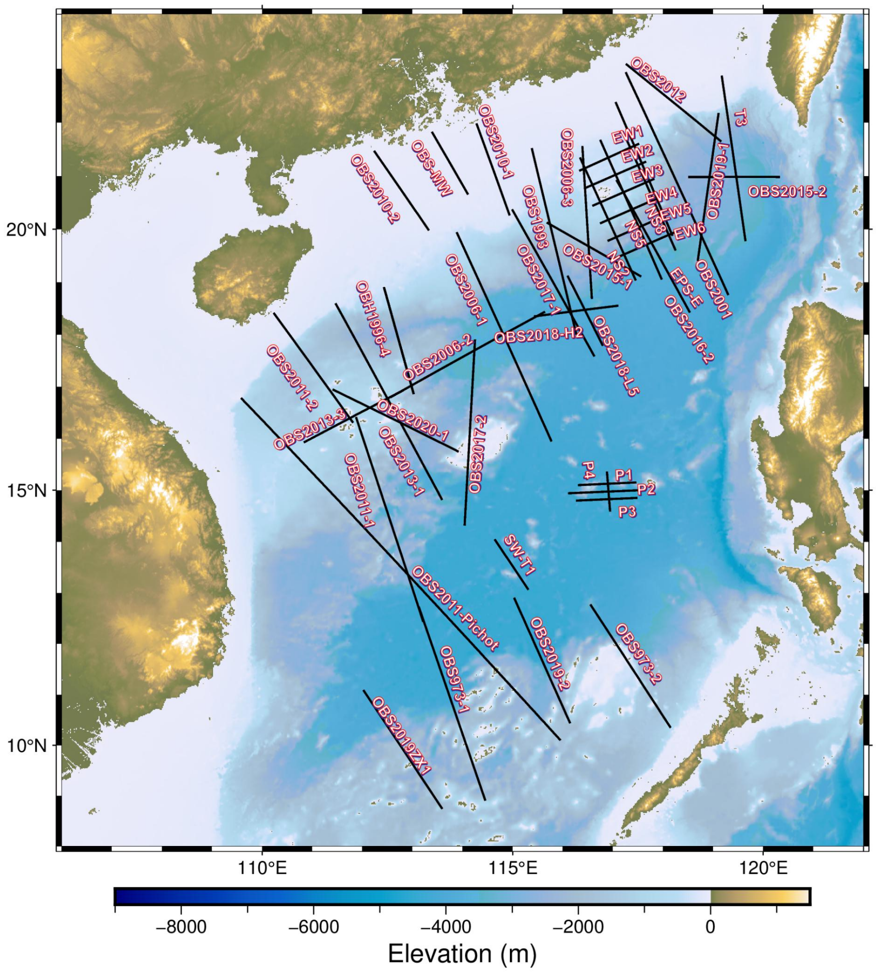

Figure 1: The distribution of forward-simulated profile data in the SCS.

Tabel 1 Forward profile data source list

OBS1993	Yan et al., 2001
EW1~EW6,NS2,NS5,NS8	Fan et al., 2017, 2019
OBS2001	Wang et al., 2006
OBS2006-1	Wu et al., 2012
OBS2006-2	Ao et al., 2012
OBS2006-3	Wei et al., 2011
OBS2010-1	Cao et al., 2014
OBS2010-2	Zhu et al., 2018
OBS2011-1	Huang et al., 2011

https://doi.org/10.5194/egusphere-2024-684
Preprint. Discussion started: 26 March 2024

OBS2011-2	Xia et al., 2022
OBS2012	Wan et al., 2017
OBS2013-1	Huang et al., 2021
OBS2013-3	Guo et al., 2016
OBS2015-1	Li et al., 2017
OBS2015-2	Liu et al., 2018
OBS2016-2	Hou et al., 2019
OBS2017-1	Zhang et al.,2023
OBS2017-2	Li et al., 2020
OBS2018-L5	Wang et al.,2022
OBS2018-H2	Zhao et al., 2022
OBS973-1	Yu et al., 2017
OBS973-2	Wei et al., 2015
OBS2019-1	Liu et al., 2021
OBS2019-2	Guo et al., 2022
OBS2011-Pichot	Pichot et al., 2014
SW-T1	Zhang et al., 2016
OBSMW	Xiong et al., 2018
P1~P4	Zhao et al., 2018
T3	Lester et al., 2014;
EPS-E	Nissen et al., 1995
OBS2019ZX1	Not yet published
OBS2020-1	Not yet published

Four auxiliary modeling datasets were used in our study, including the IGPP Global Free Air Gravity Anomaly Data_01m (Fig. 2a, Pavlis et al., 2012; Sandwell et al., 2019), EMAG2 Global Magnetic Anomaly Model_02m (Fig. 2b, Meyer et al., 2017), SRTM+ Global Topography Data Data_01m (Fig. 2c, Tozer et al., 2019), and Moho Surface Model (Fig. 2d, not yet published). These datasets were subjected to dimensionless processing before being imported as modeling auxiliary data. The SRTM+ Global Topography Data_01m and the Moho Surface Model were also used to constrain the geometric morphology of the 3D crustal model.

https://doi.org/10.5194/egusphere-2024-684
Preprint. Discussion started: 26 March 2024

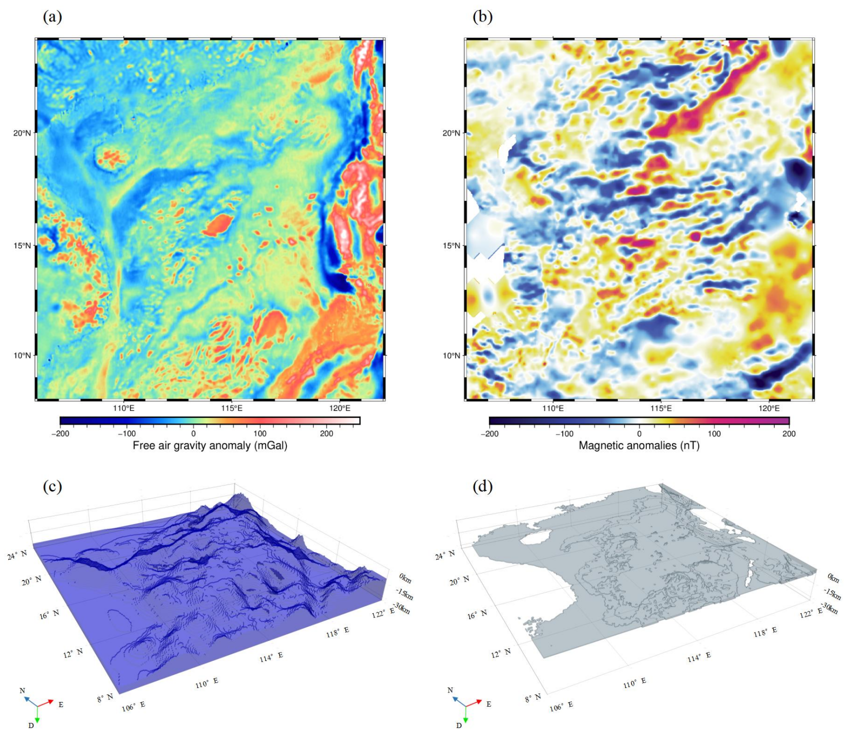

Figure 2: The auxiliary modeling datasets that used in this study. (a)IGPP Global Free Air Gravity Anomaly Data_ 01m. (b)EMAG2 Global Magnetic Anomaly Model_ 02m. (c)Moho surface model. (d)SRTM+ Global Topography Data_01m.

3. Method

The key issues to be addressed when using MPS to construct a 3D geological model are as follows: how to identify and extract the geological structural features from known geological images, i.e., TI, and how to restructure the extract the geological structures in 3D space with appropriate stochastic methods. Since the introduction of MPS by Guardiano and Srivastava (1993), many practical MPS algorithms have been proposed over the past three decades. Algorithms such as ANSIM (Yu et al., 2016), DISPAT (Arpat and Caers, 2007), GOSIM (Yang et al.,

https://doi.org/10.5194/egusphere-2024-684
Preprint. Discussion started: 26 March 2024

2016), MS-CCSIM (Tahmasebi et al., 2014), SIMPAT (Honarkhah and Caers, 2010), FILTERSIM (Zhang et al., 2006), and PCTO-SIM (Pourfard et al., 2017) extract local spatial patterns using a sliding window approach. On the other hand, methods like SNESIM (Strebelle, 2002), IMPALA (Straubhaar et al., 2011), HOSIM (Dimitrakopoulos et al., 2010; Yao et al., 2021) use data events to obtain probability distribution functions of the desired attributes at the simulation points. However, these methods only extract local spatial relationships among multiple points from the TI without considering the correlations and macro spatial distributions between geological bodies and structures. Some MPS methods divide the TI into several subregions with stationary attribute features and extract statistical information from these subregions to simulate non-stationary models (de Vris et al., 2009; Chen et al., 2015). Others incorporate soft data constraints to simulate specific statistical feature distributions (Honarkhah and Caers, 2012; Chen et al., 2015; Straubhaar et al., 2021). However, independent modeling of different blocks can lead to discontinuities or misalignments at contact boundaries. In addition, it is not easy to accurately partition a 3D simulation grid into multiple subregions based on statistical information or add 3D soft data constraints.

In recent years, deep learning (DL) has made significant progress in fields such as data mining, natural language recognition, and computer vision. The term DL was introduced to the field of machine learning in 1986 (Minar and Naher, 2018), but due to hardware performance limitations and training methods, deep learning was not widely uesd. It wasn't until 2006 that Hinton (2006) proposed a method of unsupervised layer-by-layer training of neural networks, followed by optimization using supervised backpropagation, which provided a solution to the problem of vanishing gradients in artificial neural networks, and ushered in the era of deep learning in artificial neural network research. By training deep artificial neural networks using known data, the weights of artificial neurons can be changed to obtain outputs that fit the known data based on the inputs. DL methods perform well in extracting nonlinear features from mining data (Li et al., 2021). Essentially, a DL model is an artificial neural network with multiple hidden layers. By using hidden

https://doi.org/10.5194/egusphere-2024-684
Preprint. Discussion started: 26 March 2024

layers in the model, input data is gradually transformed into combinations of low-level, mid-level, and high-level features until the output object is reached, learning the overall data features of the training dataset through multi-layer abstraction (LeCun et al., 2015). Therefore, DL has strong capabilities for recognizing and reconstructing nonlinear and nonstationary data, as well as extracting and recognizing global patterns in datasets.

Besides, research has shown that deep learning algorithms can be applied to multimodal inputs and extract overall features from the dataset (Adler et al., 2021; LeCun et al., 2015). They can effectively extract, merge, and transform features from multi-source heterogeneous data. The network uses a deep architecture for nonlinear feature extraction and can capture the relationship between different types of data, thereby improving the accuracy and robustness of the model. However, existing deep learning algorithms for multi-source heterogeneous data fusion (Bergado et al., 2021; Zhang et al., 2021) mainly classify simulation grid nodes based on multi-source heterogeneous data, and there are few algorithms that predict geological attributes such as seismic velocity structure and crustal structure at unsampled locations based on multi-source heterogeneous data. Therefore, in future research, it is necessary to design how to organize the structure of deep artificial neural networks to extract and reconstruct the mapping relationship between multi-source heterogeneous data and the geological attributes to be simulated.

This study proposes a 3D geological stochastic reconstruction algorithm that combines deep learning and with MPS. The algorithmic flow is shown in Fig. 3. After preprocessing the data, we trained two groups of multimodal artificial neural networks. The first group was used to predict the geological layer interfaces and generate the initial model, $\boldsymbol{R_0}$. After optimizing the $\boldsymbol{R_0}$ using MPS iteration, we obtained $\boldsymbol{R_1}$. Then, on the basis of $\boldsymbol{R_1}$, we used the second group of multimodal artificial neural networks to predict the P-wave velocity values at each spatial nodes. The final step is to apply a smoothing filter to output the 3D P-wave velocity structure model, $\boldsymbol{R_{final}}$.

https://doi.org/10.5194/egusphere-2024-684
Preprint. Discussion started: 26 March 2024

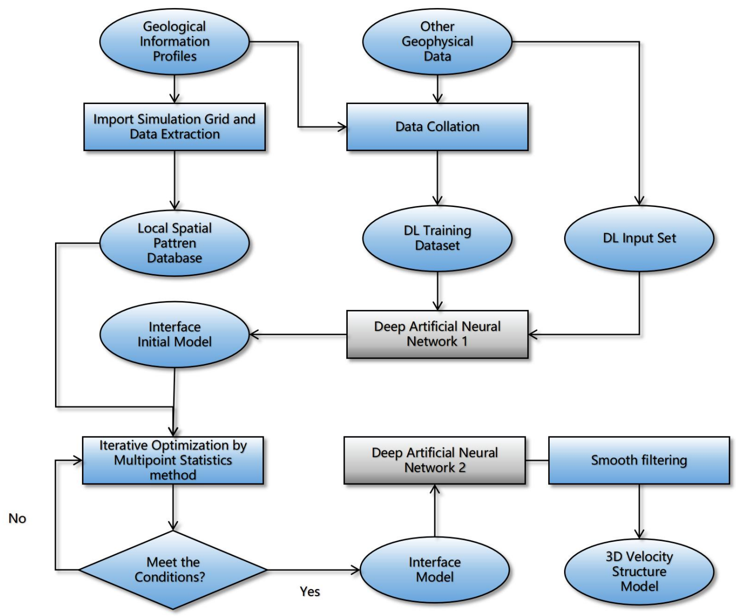

Figure 3: Algorithm flowchart.

3.1 Multimodal deep artificial neural network

The deep learning model used in this study is a multimodal deep feed-forward fully connected artificial neural network. The overall architecture is inspired by an autoencoder, as shown in Fig. 4. It takes the coordinate of spatial nodes (x, y) or (h, x, y) and the normalized value of multiple heterogeneous geophysical data corresponding to those coordinates as input. This model consists of multiple hidden layers, with the number of artificial neurons gradually decreasing in each layer, which helps to convert input data into fused feature vectors. This process achieves the fusion of multi-source heterogeneous data under a data-driven framework. Then, similar to a decoder, multiple hidden layers are used to convert feature vectors into geological information A(x, y)\` or A(h, x, y)\` for spatial nodes (x, y) or (h, x, y) by increasing the number of artificial neurons layer by layer. In this study, a hierarchical modeling strategy is combined, and two groups of multimodal deep neural networks with the

https://doi.org/10.5194/egusphere-2024-684
Preprint. Discussion started: 26 March 2024

same architecture are used in total.

The deep neural network training process in this study is as follows:

(1) Construct a multimodal deep neural network for the geological attributes that need to be reconstructed in 3D. The algorithm used in this study employs a feed-forward fully connected artificial neural network with nine hidden layers, comprising a total of 1,211,451 parameters.

(2) The training data is input into the deep neural network and the training parameters are set. Train the deep neural network by comparing the TD data A(x, y) or A(h, x, y) corresponding to spatial nodes (x, y) or (h, x, y) with A(x, y)` or A(h, x, y)`. The loss values between them are adjusted by backpropagation, which updates the weights and biases of artificial neurons in each hidden layer. The simulation is limited to a maximum of 10,000 epochs, and when the loss value is stable below a predefined threshold of 0.5×10^{-5}, the training is terminated early, resulting in the corresponding deep neural network ***M***.

In order to study the internal structure of the SCS region, it is necessary to determine the P-wave velocity values at each spatial node. However, due to the complexity of the region and the sparseness of the data, using a single deep artificial neural network for modeling can lead to difficulty in convergence. Therefore, in this study, a hierarchical modeling strategy is introduced to deal with the complexity of the data and the heterogeneity of the spatial distribution.

Hierarchical modeling is a technique that divides a large, complex system into multiple levels for more manageable modeling. By doing so, the overall complexity of the task is effectively reduced. This approach simplifies the definition and management of variables and parameters for each module, enabling separate analysis and testing. Additionally, different tasks resulting from decomposition can be parallelized, thereby improving the efficiency of model construction.

In this study, the difficulty of modeling is reduced by dividing the problem of generating unsampled P-wave velocity values into two problems and each problem is modeled using a separately trained multimodal deep artificial neural network model. The first problem involves simulating the geologic layering structure of the crust

https://doi.org/10.5194/egusphere-2024-684
Preprint. Discussion started: 26 March 2024

based on multi-source heterogeneous data. The first group of deep artificial neural network is used to generate the initial model $\boldsymbol{R_0}$ of the crust structure, which includes the 3D spatial distribution of sedimentary layers(1.7~5.5km/s), upper crust(5.5~6.5km/s) and lower crust(6.5~8km/s). The artificial artifacts in the model are then removed using a MPS optimization algorithm, resulting in the refined crust structure model $\boldsymbol{R_1}$. This process includes the following steps:

(1) Traverse the TI and assign different layer attributes to each grid node based on the range of values at that node, and get TI` with layer attributes.

(2) Use a window of size h×1×1 to traverse the TI` with layer attributes, simplifying the information on each depth plane coordinate node (x, y) into a sequence of thicknesses of the three geologic layers: the sedimentary layer, upper crust, lower crust. Normalize this sequence and use it as the label for the training dataset of the multimodal deep artificial neural network. The plane coordinate node (x, y) and the multi-source heterogeneous data $B_n(x,y)$ corresponding to that node are used as inputs.

(3) Train the multimodal deep artificial neural network using the training dataset described above to predict the thicknesses of each geologic layer at a given coordinate node. This trained network is denoted as $\boldsymbol{M_1}$.

(4) Use $\boldsymbol{M_1}$ to predict the thicknesses of the sedimentary layer, upper crust, lower crust, and mantle for all unsampled plane coordinate nodes (x, y) in the SG. Based on these thicknesses and constraints from topography and Moho depth, reconstruct the various layers in the SG and obtain the initial model $\boldsymbol{R_0}$.

(5) Combine the MPS iteration process to optimize the $\boldsymbol{R_0}$ and obtain the refined crust structure model $\boldsymbol{R_1}$.

The second problem involves the simulation of the P-wave velocity structure in each geologic layer based on multi-source heterogeneous data. Upon obtaining the refined interface model $\boldsymbol{R_1}$, the second group of multimodal deep artificial neural networks is employed to calculate the 3D P-wave velocity structure at the unsampled grid nodes between each geological interface. The final step requires integrating all models generated by the second set of neural networks to derive a comprehensive 3D

https://doi.org/10.5194/egusphere-2024-684
Preprint. Discussion started: 26 March 2024

crustal velocity structure model. This process includes several key steps:

(1) For each layer Q_n, traverse the TI` and origin TI, then obtain the spatial nodes (h, x, y) with attributes corresponding to layer Q_n and their corresponding P-wave velocity structure values from the assigned regions.

(2) Use the spatial nodes (h, x, y) and the corresponding multi-source heterogeneous data $B_n(x,y)$ as inputs. After that, employ the values A(h, x, y) of the nodes as labels to constructa training dataset for the multimodal deep artificial neural networks.

(3) Train the multimodal deep artificial neural networks with the training dataset to obtain the deep learning model $\boldsymbol{M_{Qn}}$. $\boldsymbol{M_{Qn}}$ is capable of predicting the P-wave velocity structure based on spatial coordinates and multi-source heterogeneous data.

(4) For each layer Q_n, traverse the grid nodes in the refined crust structure model $\boldsymbol{R_1}$ with attributes corresponding to Q_n. Use the coordinates (h, x, y) and their associated $B_n(x,y)$ as inputs for the multimodal deep artificial neural network $\boldsymbol{M_{Qn}}$. This will yield the P-wave velocity structure at these nodes.

(5) Repeat the above steps until all the unsampled nodes in each layer of the model are assigned values. After smoothing, the final model R_{final} of the 3D crustal velocity structure is obtained.

https://doi.org/10.5194/egusphere-2024-684
Preprint. Discussion started: 26 March 2024

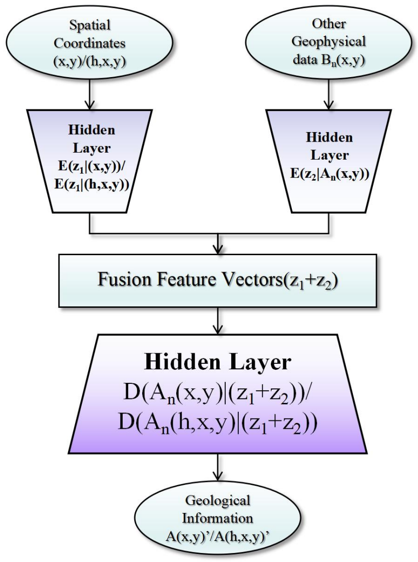

Figure 4 Network Architecture Diagram

3.2 Multipoint statistical iterative process

The results generated by the multimodal deep artificial neural network can also be regarded as one implementation. However, directly generating models often exhibits discontinuity and artifacts, and deep learning does not optimize local spatial features during simulation process. To address this, this study adopts a EM (Expectation-Maximization) iteration procedure similar to GOSIM (Yang et al., 2016; Hou et al., 2022) to improve the simulation result $\boldsymbol{R_0}$. This iteration process has made improvements in parallel optimization, optimal mode selection, and update rules. The process is illustrated in Fig. 5.

EM Iterative Algorithm Process

```
For each EM iteration process
    For each TI*:
        Define a temporary simulation grid E_z of the same size as SG to store
```

https://doi.org/10.5194/egusphere-2024-684
Preprint. Discussion started: 26 March 2024

the candidate mode coordinates obtained from TI, and define a temporary grid E_D of the same size as SG to store the distance between the corresponding candidate pattern P_{TI}^{u} and the pattern P_{R}^{u} centered on grid node $\boldsymbol{u}$.

04 Randomly assign a TI pattern P_{TI}^{u} to each node $\boldsymbol{u}$ in SG, store its coordinates in $E_z(\boldsymbol{u})$, calculate the similarity between P_{TI}^{u} and P_{R}^{u}, and then update $E_D(\boldsymbol{u})$.

05 For each E-step：

06 For each currently accessed grid node $\boldsymbol{u}$：

07 Propagation step: Calculate the similarity between the candidate patterns $P_{TI}^{u_n}$ of grid node $\boldsymbol{u_n}$ around grid node $\boldsymbol{u}$ and the patterns P_{R}^{u}, compare them with $E_D(\boldsymbol{u})$. Select the most similar pattern as the new candidate pattern, and update $E_z(\boldsymbol{u})$ and $E_D(\boldsymbol{u})$. Only three adjacent grid nodes in the top, front, left, or bottom, back, and right directions are selected as $\boldsymbol{u_n}$ in the same E step.

08 Random search step: For each grid node $\boldsymbol{u}$, set a search window centered around the position of its candidate pattern P_{TI}^{u} in TI, i.e. $E_z(\boldsymbol{u})$. In this search window, randomly extract 5 pattern $P_{TI}^{u'}$ and compare its distance to the current candidate pattern P_{R}^{u}. If there is a pattern P_{TI}^{u} that is more similar to P_{R}^{u}, it will be used as a new P_{TI}^{u} and updated $E_z(\boldsymbol{u})$ and $E_D(\boldsymbol{u})$. If not, reduce the window by the magnification and continue searching until the window size is smaller than the pattern size.

09 End

10 Change the direction of selecting adjacent nodes in the propagation step. If it is left in the current round, it will be

https://doi.org/10.5194/egusphere-2024-684
Preprint. Discussion started: 26 March 2024

changed to right in the next round.

End

End

For each currently accessed grid node ***u***（M-step）：

For each TI:

Select candidate patterns P_{TI}^{u} from TI based on E_z(***u***) and record the attribute values $C(\boldsymbol{P}_{TI_w}^{u})$ of the corresponding position of grid node ***u*** in the P_{TI}^{u}.

End

Select the most frequent occurrence from all $C(\boldsymbol{P}_{TI_w}^{u})$ to update the grid node ***u***.

End

End

*Indicates the use of parallel optimization

Figure 5 EM Iteration Algorithm Process.

4. The 3D crustal P-wave velocity structure model of the SCS

Fig. 6 shows the results of a simulation grid with dimensions of 70 × 400 × 400, and a total number of 11,200,000 grid cells. The modeling area covers the SCS region from 106°E to 122°E and 8°N to 24°N, with a vertical depth range from sea level to -35km. The vertical grid spacing is 0.5 km/grid, and the horizontal grid spacing is 0.04°/grid. The artificial neural network was trained for 10,000 epochs. On a desktop computer, it took about 30 h to build one single model.

The thickness maps of the sedimentary layer, upper crust, and lower crust in the

https://doi.org/10.5194/egusphere-2024-684
Preprint. Discussion started: 26 March 2024

modeling results are shown in Fig.9. The average thickness of the sedimentary layer is 3.64 km, with a maximum thickness of 13.0 km. Regions with relatively large thickness are concentrated near the Yinggehai Basin (Fig. 6b). The average thickness of the upper crust model is 6.95km, while the average thickness of the lower crust model is 7.0 km. A clear thinning phenomenon was observed in the SCS basin, with minimum thicknesses of 0.5 km and 1 km, respectively (Figs. 6c and 6d).

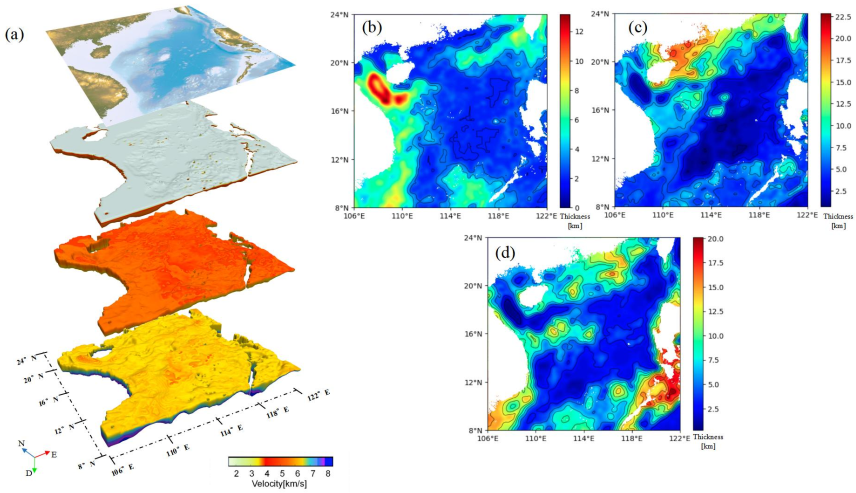

Figure 6 (a) The sedimentary layer, upper crust and lower crust in the modeling results are displayed, and (b) (c) (d) their corresponding thicknesses are displayed respectively.

Fig. 7 depict the depth maps of the sedimentary interface, Moho interface, crustal top interface, and HVL (High Velocity Layer) top interface in the modeling results. The sedimentary interface in the modeling results indicate that the sedimentary interface within the SCS basin region has a deeper average depth of 1.61km, with a maximum depth of 5.0km. The crustal top interface also exhibits similar characteristics, with an overall average depth of 5.24km. The deepest point is located near the Yinggehai Basin, reaching a maximum depth of 14.0km.In contrast, both the HVL top interface and Moho interface display similiar characteristics. The HVL top interface is shallower in the SCS basin and deeper in other areas. The overall average

https://doi.org/10.5194/egusphere-2024-684
Preprint. Discussion started: 26 March 2024

depth of the HVL top interface is 17.94m, while the Moho interface has an overall average depth of 21.0km. From the outer edges to the central basin, the depth of the Moho interface decreases abruptly from around 20km to approximately 10km. Overall, the 3D crustal model of the SCS aligns well with previous studies in terms of the velocity structure.

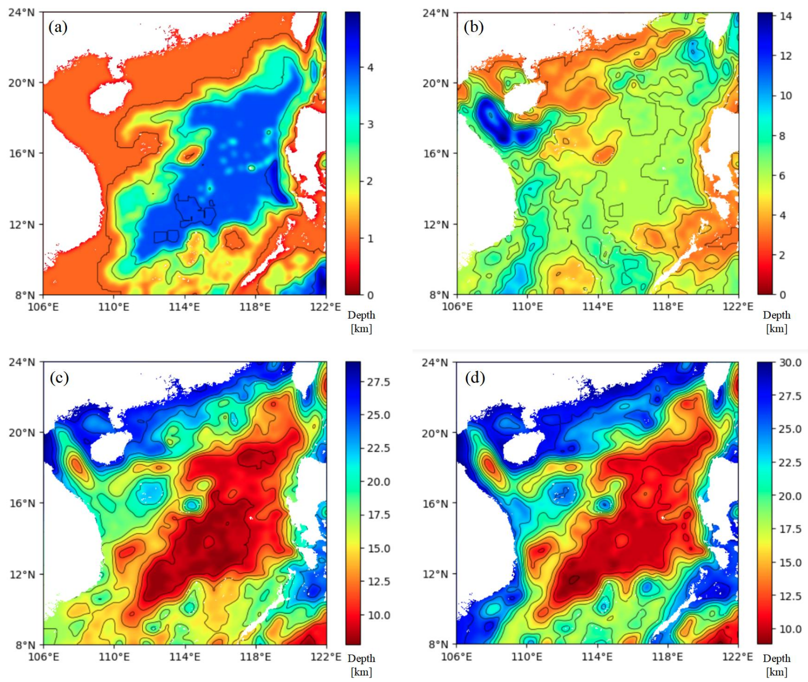

Figure 7 The sedimentary interface (a) , the crustal top interface (b), the HVL top interface (c) and the Moho surface(d) in the modeling results.

5. Discussion

As shown in Fig. 8 and 9, the deep learning neural network, trained with multisource heterogeneous data, demonstrates lower loss values, higher accuracy, or

https://doi.org/10.5194/egusphere-2024-684
Preprint. Discussion started: 26 March 2024

lower average absolute error in predicting velocity structures. Moreover, these models requires relatively fewer training iterations to reach a relatively stable state. Compared with the curves of loss values, error value, and accuracy obtained under the same parameters without utilizing multi-source heterogeneous data, the integration of multi-source heterogeneous data reduces the fluctuation range of the curves. Furthermore, we calculated several fitting goodness-of-fit parameters for the model. Under the premise of using heterogeneous data from multiple sources, the model achieved a goodness-of-fit of 0.96029, which is better than the result of 0.95717 obtained without using heterogeneous data. The prediction results showed that the MSE was 0.16505, MAE was 0.15696 and MAPE was 0.0307. Compared with the modeling results without using heterogeneous data, these values were reduced by 0.01151, 0.00915 and 0.00213 respectively. This shows that the model has superior performance in reducing errors and significantly improving prediction accuracy. These results show that the multimodal deep artificial neural network architecture developed in this study can effectively integrate diverse geophysical data from SCS, thereby improving the performance of 3D geological information modeling algorithms.

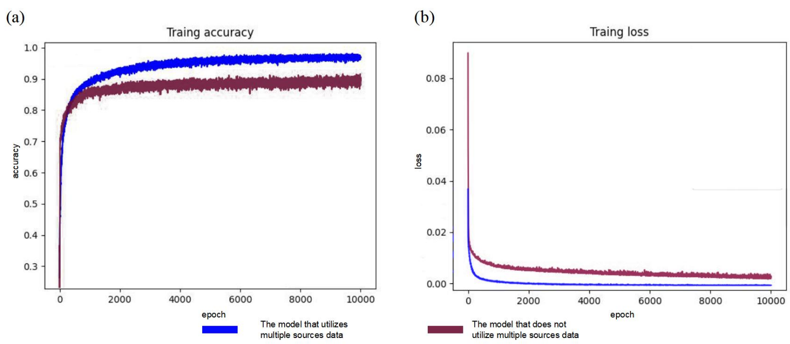

Figure 8 The curve graphs depict the variation of algorithm accuracy (a) and training loss (b) with increasing training epochs for a deep artificial neural network simulating geological stratigraphy.

https://doi.org/10.5194/egusphere-2024-684
Preprint. Discussion started: 26 March 2024

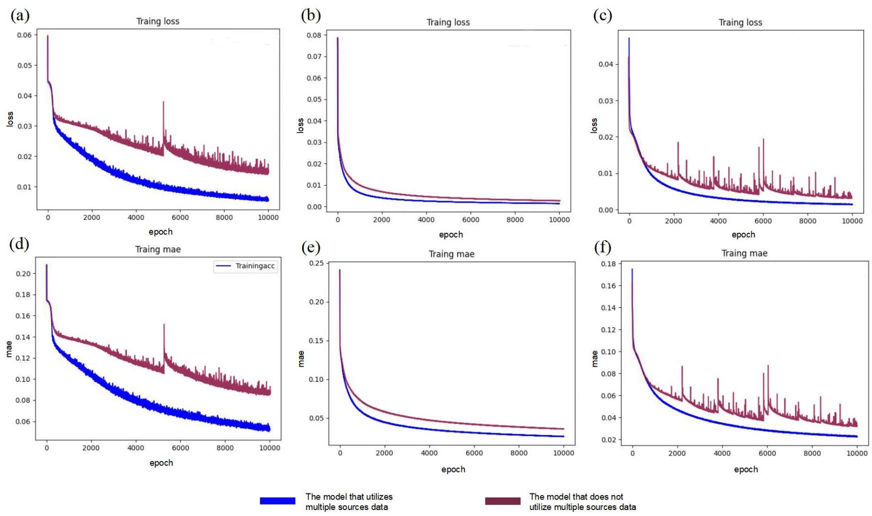

Figure 9 The curve graph illustrates the variation of training loss and mean absolute error (MAE) with increasing training epochs and iterations, respectively, for a deep artificial neural network simulating the internal velocity structure of the sedimentary layers (a, d), upper crust (b, e), and lower crust (c, f).

To verify the accuracy of the model, the multi-source heterogeneous data fusion model developed in this study was compared with the model that without using multi-source heterogeneous data (Fig. 10b), the Kriging interpolation model (Fig. 10c) and the MPS interpolation model(Fig. 10d) . From a visual point of view, compared with the model built in this study (Fig. 10a), the Kriging interpolation result is excessively smooth and lacks local details. There are significant differences in terrain variations and Moho depth compared to existing models, and there are also numerous artificial artifacts. In the model constructed without using multi-source heterogeneous data and the model constructed by MPS, both the upper crust and lower crust have a large number of discontinuities and abrupt thickenings. The model constructed by MPS even has stratigraphic misalignment, which is clearly inconsistent with previous knowledge.

Under the premise of not including OBS2017-2 data (Li et al., 2021), this study

https://doi.org/10.5194/egusphere-2024-684
Preprint. Discussion started: 26 March 2024

constructed the above four types of models mentioned above and compared the extracted profiles at that location (Fig.11). After calculating the residuals between the profile of the multi-source heterogeneous fusion model (Fig. 11c) and OBS2017-2 data (Fig. 11a), the root mean square error (RMSE) was found to be 0.6281 km/s, and the Jensen-Shannon divergence (JS divergence) was 0.03484. For the profile of the model without integrating multi-source heterogeneous data (Fig. 11e), the RMSE was 0.8246 km/s and the JS divergence was 0.05443, while for the Kriging interpolation result（Fig. 11g）, the RMSE was 0.8723 km/s and the JS divergence was 0.05881. The latter three models clearly deviate more from the actual conditions. Similarly, the comparisons without including OBS2012-2 data and OBS973-2 are shown in Appendices. This verifies that the model constructed by the algorithm proposed in this study is closer to the reality.

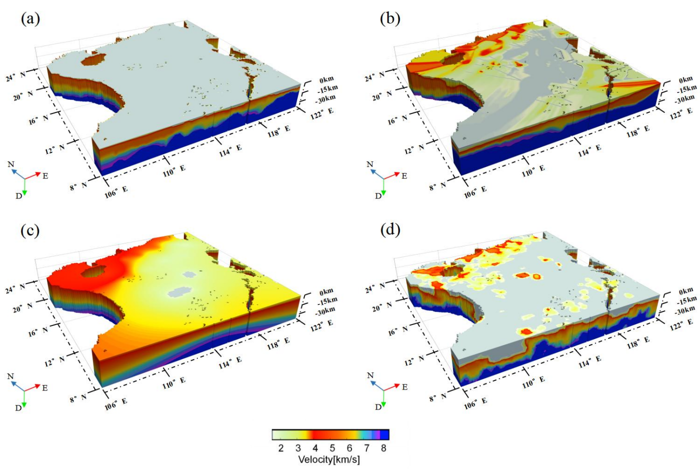

Figure 10 The modeling results of the SCS model constructed without integrating multi-source heterogeneous data. (a) is the overall 3D velocity structure model. (b) represents the result of modeling for sedimentary layer, (c) for the upper crust, and (d) and (e) respectively represent the lower crust and Mantle in the modeling results.

https://doi.org/10.5194/egusphere-2024-684
Preprint. Discussion started: 26 March 2024

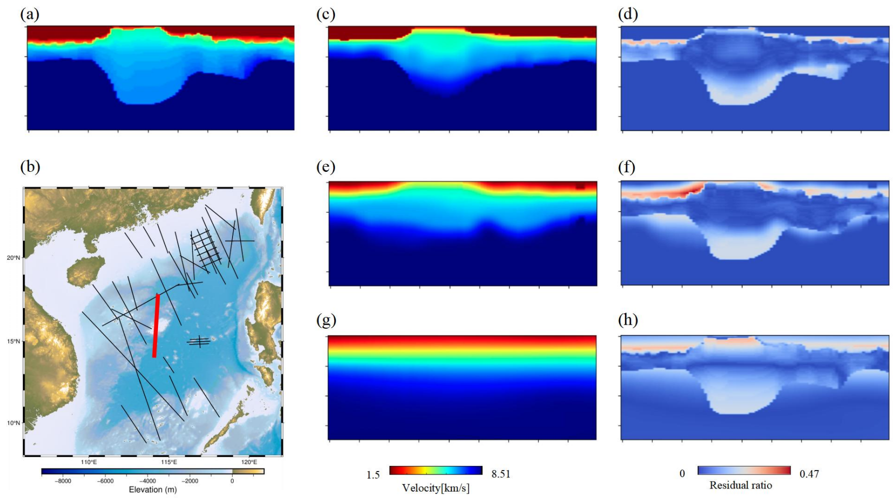

Figure 11 OBS2017-2 forward modeling profile. (b) Schematic diagram of the location of OBS2017-2 profile data, where the red line represents the OBS2017-2 profile. (c) (e) (g) are the profiles of OBS2017-2 position in the model constructed by using multi-source heterogeneous data, not using multi-source heterogeneous data, and Kriging interpolation respectively, and (d) (f) (h) are the residual maps of these profiles and OBS2017-2 profile data.

Attribute proportion statistics refer to the proportions of different geological attributes in the model, which intuitively reflect the differences between the modeling results and known data in terms of geologicial attributes. Fig. 12 shows the comparison of attribute proportions for various geologic layers in the 3D model, which are classified according to velocity. Compared with the Kriging interpolation method and MPS method, the modeling results of the new method are more similar to the known data in terms of attribute proportions. The use or non-use of multi-source heterogeneous data has little impact on the attribute proportions in the simulation results.

https://doi.org/10.5194/egusphere-2024-684
Preprint. Discussion started: 26 March 2024

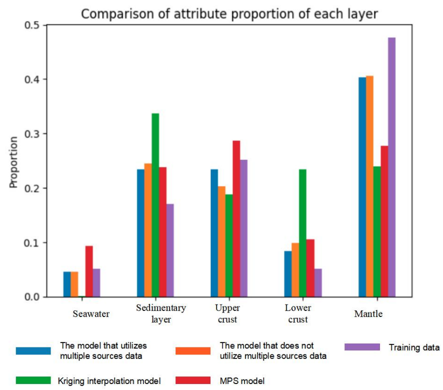

Figure 12 Comparison of attribute proportions.

By calculating the average thickness of the geological layer (Fig. 13a), maximum thickness (Fig. 13b), minimum thickness (Fig. 13c), average elevation of the top surface (Fig. 13d), maximum elevation of the top surface (Fig. 13e), minimum elevation of the top surface (Fig. 13f), average elevation of the bottom surface (Fig. 13g), maximum elevation of the bottom surface (Fig. 13h) and minimum elevation of the bottom surface (Fig. 13i), it is possible to visually evaluate the similarities and differences between the simulation results and the known data at the level of the geological layers. The traditional Kriging interpolation method tends to simulate the geological interfaces as curved surfaces, so in general, the simulation results of the Kriging interpolation method show that the top surfaces of the geologic layers are shallower and the bottom surfaces are deeper. Compared with the Kriging interpolation model, MPS interpolation model and the simulation result without utilizing multiple sources of heterogeneous data, the modeling results obtained by integrating multi-source hetereogeneous data showed greater consistency with the training data in terms of statistical indicators, and they were more consistent with actual conditions.

https://doi.org/10.5194/egusphere-2024-684
Preprint. Discussion started: 26 March 2024

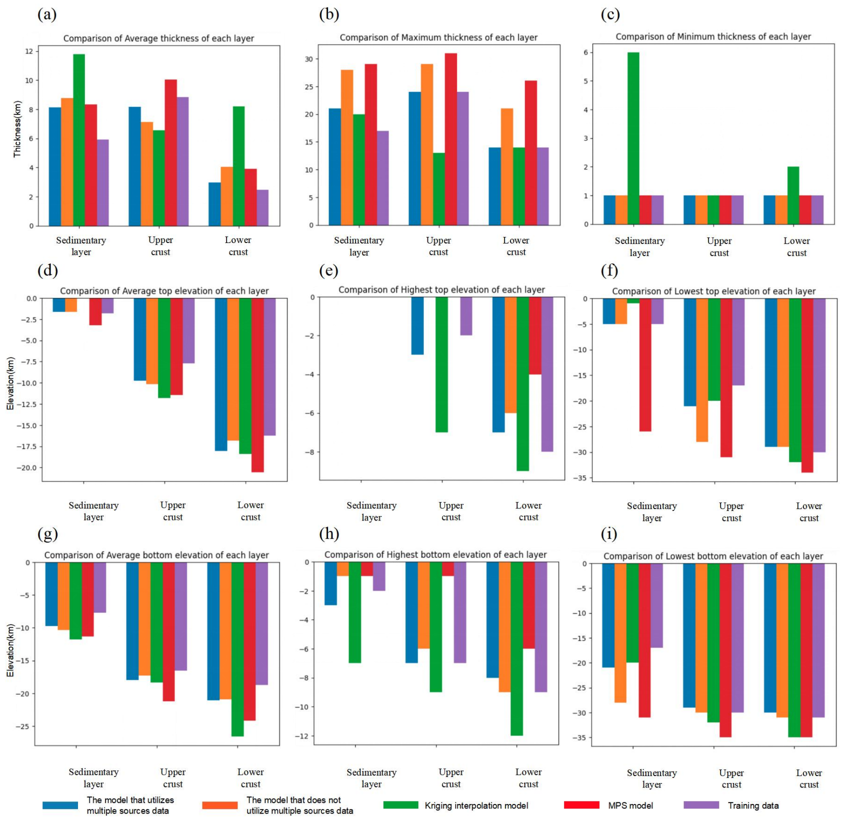

Figure 13 Comparison of geologic layer structure thickness (a-c), top interface depths (d-f), and bottom interface depths (g-i) displaying the statistics of average, maximum, and minimum values for each layer in the simulation results.

The variogram function can effectively extract and represent the spatial structure and randomness of regionalized variables (Chiles et al., 2012; Pyrcz et al., 2014). As shown in Fig. 14, the variation function curves of the modeling results fused with multi-source heterogeneous data are distributed in the middle of the variation function curve set of 44 forward profile data, which indicating that the variogram curves of the modeling results obtained by integrating multi-source heterogeneous data are more similar to the training data than other results.

https://doi.org/10.5194/egusphere-2024-684
Preprint. Discussion started: 26 March 2024

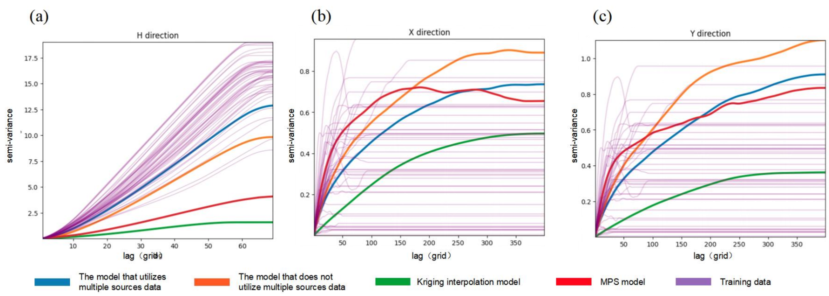

Figure 14 Comparison of Variation Function Graphs of Simulation Results.(a), (b) and (c) represent the statistical results of depth, east-west, and north-south components, respectively. Due to the different distribution directions of 44 OBS profiles, the statistical direction of the variation function of the training data in (b) and (c) corresponds to the direction of the forward profile.

Fig. 15a reveals that, although the model constructed by DeepLearning has an overall trend , it still exhibits some artificial artifacts and discontinuous structures. The red circle highlights the steep velocity transition. These observations show that the proposed deep artificial neural network can capture the global spatial characteristics of known geological objects but lacks precise characterization of local spatial features. On the other hand, the iterative MPS algorithm effectively reduces or eliminates the artificial artifacts in the model(Fig 15b), and provides fine local characterization based on the local spatial features obtained from TIs, while correcting some local errors.

https://doi.org/10.5194/egusphere-2024-684
Preprint. Discussion started: 26 March 2024

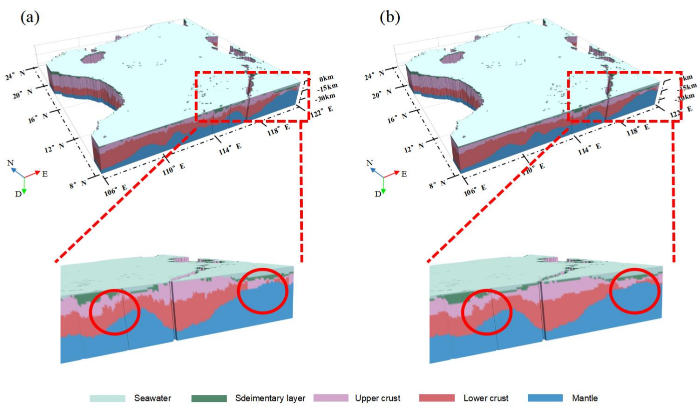

Figure 15 Comparison of the simulation result without using the iterative algorithm (a) and simulation result after using the MPS iterative algorithm (b). The red circles highlight the areas where the artificial artifacts in the model have been corrected after the iteration.

By visually inspecting and comparing the geological statistical parameters and profile sections, we can initial assess that our 3D crustal velocity structure model of the SCS is reasonably reliable and superior to traditional 3D model constructed using Kriging interpolation, model that do not utilize heterogeneous multi-source data, and model constructed by MPS. The model successfully reconstructs the global spatial characteristics of the crustal P-wave velocity structure, which aligns well with our prior knowledge acquired from the SCS. The model shows better consistency with the original data in terms of attribute proportions, variogram statistics, geological interface elevation, and thickness statistics.

During the 3D random simulation process, the availability of conditional data directly influences the diversity of spatial distribution patterns. The more data we have, the greater the constraints imposed on the simulation by known information, thereby bringing the model closer to reality. Multimodal deep artificial neural networks, when trained with a larger dataset or additional modalities, exhibit superior generalization and stability. Furthermore, an increased amount of target modeling data offers more local spatial patterns for multipoint statistics. This

https://doi.org/10.5194/egusphere-2024-684
Preprint. Discussion started: 26 March 2024

allows the 3D geological model to better capture local spatial features that correspond to real-world situations during iterative optimization. By gathering more heterogeneous data from various sources, the proposed algorithm can update, calibrate, and refine previously constructed 3D geological models, enhancing its adaptability to new data distributions.

It is worth noting that the data used to train the multimodal deep artificial neural network is not limited to the data in study area. In subsequent work, it can also be attempted to use data from other regions to provide references for the construction of geological models in the study area, such as seismic exploration profiles and geophysical data on land, seismic exploration profiles and geophysical data on other oceans, etc. Different regions may share certain similarities and correlations in geological conditions, which can provide references for building higher-quality models. Theoretically, the use of cross-regional data can imporve the accuracy and generalization abilities of the deep artificial neural networks, allowing the algorithm to extract and summarize more universal geological features or patterns from the data. This in turn improves the understanding and predictive ability of the algorithm with respect to the geological conditions of the study area.

Apart from the P-wave velocity structure, other attributes can also be used as target modeling data for this algorithm, such as S-wave velocity structure, density structure, etc. By amassing and organizing data into datasets, this algorithm is capable of constructing corresponding 3D models of geophysical and geological attributes. The construction of these geological and geophysical attribute models can also provide foundational information for various fields including geological research, resource exploration, seismic activity, and Earth evolution studies.

6. Conclusion

Our research introduces a novel 3D modeling technique that merges multimodal deep learning with MPS. This method aims to overcome the challenges associated with reconstructing non-stationary features of geological structures and integrating heterogeneous data from multiple sources. By leveraging multimodal deep learning, it amalgamates diverse data sources to enhance the precision of 3D model construction and minimize modeling ambiguity. The hierarchical modeling strategy employed during the process simplifies the training of deep learning networks to convergence, ensuring that the final model results take into account both local and global spatial features of the original data. This approach yields superior alignment with prior knowledge and raw data.

Based on this new method and the collected data, the research has successfully constructed a high-quality 3D crustal P-wave velocity structure model of the SCS. A range of indicators, including the proportions of lithological attributes, leave-one-out comparisons, and variogram analyses, have been employed to validate both the feasibility of the new algorithm and the reliability of the crustal model of the SCS. The model provides an intuitive representation of spatial distribution characteristics of geological structures, thereby serving as a robust data foundation for researchers to gain a more comprehensive understanding of geological evolution processes of the SCS.

Funding Declaration

This research was funded by China National Key R&D Program Project [2022YFC3102200] and National Natural Science Foundation of China [42076071]

Competing Interest Declaration

All authors declare that they have no commercial or associative interest that represents a conflict of interest connected with the work submitted.

https://doi.org/10.5194/egusphere-2024-684
Preprint. Discussion started: 26 March 2024

Data availability Statement

The dataset generated in this study is not currently publicly available. However, if needed, it can be obtained by contacting the respective author. Interested researchers are encouraged to send their requests and the reasons for their requests to liuhg233@scsio.ac.cn.

Author Contribution declaration

The contributions of the authors to this manuscript are as follows: Hengguang Liu was responsible for developing the methodologies, processing data, programming algorithms, drawing figures, and drafting the initial manuscript. Shaohong Xia provided the central research ideas and overall planning, guided the methodologies and results, managed the data and project, secured funding, and revised the initial draft. Chaoyan Fan participated in discussions regarding the methodologies and results, and also contributed to revising the initial draft. Changrong Zhang also engaged in the method and result discussions and made revisions to the initial draft.

References

1. Adler, A., Araya-Polo, M., and Poggio, T.: Deep Learning for Seismic Inverse Problems: Toward the Acceleration of Geophysical Analysis Workflows, Ieee Signal Processing Magazine, 38, 89-119, 10.1109/msp.2020.3037429, 2021.
2. Ao, W., Zhao, M., Qiu, X., Ruan, A., and Li, J.: Crustal Structure of the Northwest Sub-Basin of the South China Sea and Its Tectonic Implication, Earth Science, 37, 779-790, 2012.
3. Arpat, G. B.: Sequential simulation with patterns, 2005.
4. Barnes, C., Shechtman, E., Finkelstein, A., and Goldman, D. B.: PatchMatch: A Randomized Correspondence Algorithm for Structural Image Editing, Acm Transactions on Graphics, 28, 10.1145/1531326.1531330, 2009.
5. Bergado, J. R., Persello, C., Reinke, K., and Stein, A.: Predicting wildfire burns from big geodata using deep learning, Safety Science, 140,

10.1016/j.ssci.2021.105276, 2021.
6. Cao, J.-H., Sun, J.-L., Xu, H.-L., and Xia, S.-H.: Seismological features of the littoral fault zone in the Pearl River Estuary, Chinese Journal of Geophysics-Chinese Edition, 57, 498-508, 10.6038/cjg20140215, 2014.
7. Chen, Q., Liu, G., Ma, X., Li, X., and He, Z.: 3D stochastic modeling framework for Quaternary sediments using multiple-point statistics: A case study in Minjiang Estuary area, southeast China, Computers & Geosciences, 136, 10.1016/j.cageo.2019.104404, 2020.
8. Chen, G., Zhao, F., Wang, J., Zheng, H., Yan, Y., Wang, A., Li, J., and Hu, Y.: Regionalized multiple-point stochastic geological modeling: A case from braided delta sedimentary reservoirs in Qaidam Basin, NW China, Petroleum Exploration and Development, 42, 697-704, 10.1016/s1876-3804(15)30065-3, 2015.
9. Cui, Z., Chen, Q., and Liu, G.: Characterization of Subsurface Hydrogeological Structures With Convolutional Conditional Neural Processes on Limited Training Data, Water Resources Research, 58, 10.1029/2022wr033161, 2022.
10. Dimitrakopoulos, R., Mustapha, H., and Gloaguen, E.: High-order Statistics of Spatial Random Fields: Exploring Spatial Cumulants for Modeling Complex Non-Gaussian and Non-linear Phenomena, Mathematical Geosciences, 42, 65-99, 10.1007/s11004-009-9258-9, 2010.
11. Fan, C., Xia, S., Cao, J., Zhao, F., Sun, J., Wan, K., and Xu, H.: Lateral crustal variation and post-rift magmatism in the northeastern South China Sea determined by wide-angle seismic data, Marine Geology, 410, 70-87, 10.1016/j.margeo.2018.12.007, 2019.
12. Fan, C., Xia, S., Zhao, F., Sun, J., Cao, J., Xu, H., and Wan, K.: New insights into the magmatism in the northern margin of the South China Sea: Spatial features and volume of intraplate seamounts, Geochemistry Geophysics Geosystems, 18, 2216-2239, 10.1002/2016gc006792, 2017.
13. Gao, J., Wu, S., McIntosh, K., Mi, L., Liu, Z., and Spence, G.: Crustal structure and extension mode in the northwestern margin of the South China Sea, Geochemistry Geophysics Geosystems, 17, 2143-2167, 10.1002/2016gc006247, 2016.
14. Guardiano, F. B. and Srivastava, R. M.: MULTIVARIATE GEOSTATISTICS - BEYOND BIVARIATE MOMENTS, 4th International Geostatics Congress : Troia 92, Troy, Portugal, 1993
15. Sep, WOS:A1993BY18R00012, 133-144, 1993.
16. Guo, J., Qiu, X., Li, Z., and Huang, H.: Data processing and phase identification of OBS2019-2 in Nansha Block, Journal of Tropical Oceanography, 41, 43-56, 2022.
17. Guo, X.-R., Zhao, M.-H., Huang, H.-B., Qiu, X.-L., Wang, J., He, E.-Y., and Zhang, J.-Z.: Crustal structure of Xisha block and its tectonic attributes, Chinese Journal of Geophysics-Chinese Edition, 59, 1414-1425, 10.6038/cjg20160422, 2016.
18. Hansen, T. M., Le Thanh, V., Mosegaard, K., and Cordua, K. S.: Multiple point statistical simulation using uncertain (soft) conditional data, Computers & Geosciences, 114, 1-10, 10.1016/j.cageo.2018.01.017, 2018.
19. Hinton, G. E. and Salakhutdinov, R. R.: Reducing the dimensionality of data with

neural networks, Science, 313, 504-507, 10.1126/science.1127647, 2006.

20. Honarkhah, M.: Stochastic Simulation of Patterns Using Distance-Based Pattern Modeling, 2011.
21. Honarkhah, M. and Caers, J.: Stochastic Simulation of Patterns Using Distance-Based Pattern Modeling, Mathematical Geosciences, 42, 487-517, 10.1007/s11004-010-9276-7, 2010.
22. Hou, W., Liu, H., Zheng, T., Chang, H., and Xiao, F.: Extended GOSIM: MPS-Driven Simulation of 3D Geological Structure Using 2D Cross-Sections, Earth and Space Science, 9, 10.1029/2021ea001801, 2022.
23. Hou, W., Chen, Y., Liu, H., Xiao, F., Liu, C., and Wang, D.: Reconstructing Three-dimensional geological structures by the Multiple-point statistics method coupled with a deep neural network: A case study of a metro station in Guangzhou, China, Tunnelling and Underground Space Technology, 136, 10.1016/j.tust.2023.105089, 2023.
24. Hou, J., Jin, J., Lin, H., Liu, Z., Fu, J., Feng, F., and Ieee: An Overview of Deep Learning Techniques for Inverse Design of Metasurface, IEEE MTT-S International Conference on Numerical Electromagnetic and Multiphysics Modeling and Optimization (NEMO), Winnipeg, CANADA, 2023 Jun 28-30, WOS:001050927700030, 110-113, 10.1109/nemo56117.2023.10202522, 2023.
25. Huang, H., Klingelhoefer, F., Qiu, X., Li, Y., and Wang, P.: Seismic Imaging of an Intracrustal Deformation in the Northwestern Margin of the South China Sea: The Role of a Ductile Layer in the Crust, Tectonics, 40, 10.1029/2020tc006260, 2021.
26. Huang, H.-B., Qiu, X.-L., Xu, H.-L., Zhao, M.-H., Hao, T.-Y., Xu, Y., and Li, J.-B.: Preliminary results of the earthquake observation and the onshore-offshore seismic experiments on Xisha Block, Chinese Journal of Geophysics-Chinese Edition, 54, 3161-3170, 10.3969/j.issn.0001-5733.2011.12.016, 2011.
27. Kaufmann, O. and Martin, T.: 3D geological modelling from boreholes, cross-sections and geological maps, application over former natural gas storages in coal mines, Computers & Geosciences, 34, 278-290, 10.1016/j.cageo.2007.09.005, 2008.
28. LeCun, Y., Bengio, Y., and Hinton, G.: Deep learning, Nature, 521, 436-444, 10.1038/nature14539, 2015.
29. Lester, R., Van Avendonk, H. J. A., McIntosh, K., Lavier, L., Liu, C. S., Wang, T. K., and Wu, F.: Rifting and magmatism in the northeastern South China Sea from wide-angle tomography and seismic reflection imaging, Journal of Geophysical Research-Solid Earth, 119, 2305-2323, 10.1002/2013jb010639, 2014.
30. Li, L., Srinivasan, S., Zhou, H., and Gomez-Hernandez, J. J.: Simultaneous Estimation of Geologic and Reservoir State Variables Within an Ensemble-Based Multiple-Point Statistic Framework, Mathematical Geosciences, 46, 597-623, 10.1007/s11004-013-9504-z, 2014.
31. Li, T., Zuo, R., Xiong, Y., and Peng, Y.: Random-Drop Data Augmentation of Deep Convolutional Neural Network for Mineral Prospectivity Mapping, Natural

https://doi.org/10.5194/egusphere-2024-684
Preprint. Discussion started: 26 March 2024

Resources Research, 30, 27-38, 10.1007/s11053-020-09742-z, 2021.

32. Li, Y., Yan, P., Wang, Y., and Zhong, G.: Deep crustal structure revealed by ocean bottom seismic profile OBS2015-1 in southwestern Dongsha waters, Journal of Tropical Oceanography, 36, 83-92, 2017.
33. Li, Y., Grevemeyer, I., Huang, H., Qiu, X., and Xu, Z.: Seismic Constraint From <i>V</i>_p/<i>V</i>_s Ratios on the Structure and Composition Across the Continent-Ocean Transition Zone, South China Sea, Geophysical Research Letters, 48, 10.1029/2021gl094656, 2021.
34. Li, Y., Teng, Q., He, X., Feng, J., and Xiong, S.: Super-dimension-based three-dimensional nonstationary porous medium reconstruction from single two-dimensional image, Journal of Petroleum Science and Engineering, 174, 968-983, 10.1016/j.petrol.2018.12.004, 2019.
35. Li, Y., Huang, H., Qiu, N., Du, F., Long, G., Zhang, H., Chen, H., and Wang, Q.: Wide-angle and multi-channel seismic surveys in Zhongsha waters, Chinese Journal of Geophysics-Chinese Edition, 63, 1523-1537, 10.6038/cjg2020N0259, 2020.
36. Lindsay, M. D., Ailleres, L., Jessell, M. W., de Kemp, E. A., and Betts, P. G.: Locating and quantifying geological uncertainty in three-dimensional models: Analysis of the Gippsland Basin, southeastern Australia, Tectonophysics, 546, 10-27, 10.1016/j.tecto.2012.04.007, 2012.
37. Liu, G.-D.: Intensify the research on continental margin of South China Sea, Chinese Journal of Geophysics-Chinese Edition, 54, 2991-2992, 10.3969/3.issn.0001-5733.2011.12.001, 2011.
38. Liu, S., Zhao, M., Sibuet, J.-C., Qiu, X., Wu, J., Zhang, J., Chen, C., Xu, Y., and Sun, L.: Geophysical constraints on the lithospheric structure in the northeastern South China Sea and its implications for the South China Sea geodynamics, Tectonophysics, 742, 101-119, 10.1016/j.tecto.2018.06.002, 2018.
39. Liu, Y., Li, C.-F., Wen, Y., Yao, Z., Wan, X., Qiu, X., Zhang, J.-z., Abbas, A., Peng, X., and Li, G.: Mantle serpentinization beneath a failed rift and post-spreading magmatism in the northeastern South China Sea margin, Geophysical Journal International, 225, 811-828, 10.1093/gji/ggab006, 2021.
40. Ma, B., Wu, S., Mi, L., Luedmann, T., Gao, J., and Gao, W.: Mixed Carbonate-Siliciclastic Deposits in a Channel Complex in the Northern South China Sea, Journal of Earth Science, 29, 707-720, 10.1007/s12583-018-0830-4, 2018.
41. Manuel de Vries, L., Carrera, J., Falivene, O., Gratacos, O., and Jan Slooten, L.: Application of Multiple Point Geostatistics to Non-stationary Images, Mathematical Geosciences, 41, 29-42, 10.1007/s11004-008-9188-y, 2009.
42. Mariethoz, G., Renard, P., and Straubhaar, J.: The Direct Sampling method to perform multiple-point geostatistical simulations, Water Resources Research, 46, 10.1029/2008wr007621, 2010.
43. Meyer, B., Saltus, R., and Chulliat, A. EMAG2V3: earth magnetic anomaly Grid (2-arc-minute resolution). Version 3. NOAA national centers for environmental information, 2017

44. Mosammam, A. M.: Geostatistics: modeling spatial uncertainty, 2nd edition, Journal of Applied Statistics, 40, 923-923, 10.1080/02664763.2012.750474, 2013.
45. Nissen, S. S., Hayes, D. E., Buhl, P., Diebold, J., Yao, B. C., Zeng, W. J., and Chen, Y. Q.: DEEP PENETRATION SEISMIC-SOUNDINGS ACROSS THE NORTHERN MARGIN OF THE SOUTH-CHINA-SEA, Journal of Geophysical Research-Solid Earth, 100, 22407-22433, 10.1029/95jb01866, 1995.
46. Pavlis, N. K., Holmes, S. A., Kenyon, S. C., and Factor, J. K.: The Development and Evaluation of the Earth Gravitational Model 2008 (EGM2008) (vol 117, B04406, 2012), Journal of Geophysical Research-Solid Earth, 118, 2633-2633, 10.1002/jgrb.50167, 2013.
47. Piao, Q., Zhang, B., Zhang, R., Geng, M., and Zhong, G.: Continent-ocean transition in the northern South China Sea by high-quality deep reflection seismic data, Chinese Journal of Geophysics-Chinese Edition, 65, 2546-2559, 10.6038/cjg2022P0663, 2022.
48. Pichot, T., Delescluse, M., Chamot-Rooke, N., Pubellier, M., Sun, G., Meresse, F., Sun, G., Savva, D., Wong, K. P., Watremez, L., and Auxietre, J. L.: Deep crustal structure of the conjugate margins of the SW South China Sea from wide-angle refraction seismic data, Marine and Petroleum Geology, 58, 627-643, 10.1016/j.marpetgeo.2013.10.008, 2014.
49. Pourfard, M., Abdollahifard, M. J., Faez, K., Motamedi, S. A., and Hosseinian, T.: PCTO-SIM: Multiple-point geostatistical modeling using parallel conditional texture optimization, Computers & Geosciences, 102, 116-138, 10.1016/j.cageo.2016.12.012, 2017.
50. Qu, H., Pan, M., Liu, X., and Yu, C.: Urban 3-D geological modeling and its application to urbanization, Geological Bulletin of China, 34, 1350-1358, 2015.
51. Sandwell, D. T., Harper, H., Tozer, B., and Smith, W. H. F.: Gravity field recovery from geodetic altimeter missions, Advances in Space Research, 68, 1059-1072, 10.1016/j.asr.2019.09.011, 2021.
52. Song, W., Yao, J., Ma, J., Couples, G. D., Li, Y., and Sun, H.: Pore-scale numerical investigation into the impacts of the spatial and pore-size distributions of organic matter on shale gas flow and their implications on multiscale characterisation, Fuel, 216, 707-721, 10.1016/j.fuel.2017.11.114, 2018.
53. Straubhaar, J. and Renard, P.: Conditioning Multiple-Point Statistics Simulation to Inequality Data, Earth and Space Science, 8, 10.1029/2020ea001515, 2021.
54. Straubhaar, J., Renard, P., Mariethoz, G., Froidevaux, R., and Besson, O.: An Improved Parallel Multiple-point Algorithm Using a List Approach, Mathematical Geosciences, 43, 305-328, 10.1007/s11004-011-9328-7, 2011.
55. Tahmasebi, P., Sahimi, M., and Caers, J.: MS-CCSIM: Accelerating pattern-based geostatistical simulation of categorical variables using a multi-scale search in Fourier space, Computers & Geosciences, 67, 75-88, 10.1016/j.cageo.2014.03.009, 2014.
56. Taylor, B., Hayes, and D. E. Origin and history of the South China Sea basin. Washington DC American Geophysical Union Geophysical Monograph

Series, 27, 23-56, 1983

57. Tozer, B., Sandwell, D. T., Smith, W. H. F., Olson, C., Beale, J. R., and Wessel, P.: Global Bathymetry and Topography at 15 Arc Sec: SRTM15+, Earth and Space Science, 6, 1847-1864, 10.1029/2019ea000658, 2019.
58. Wan, K., Xia, S., Cao, J., Sun, J., and Xu, H.: Deep seismic structure of the northeastern South China Sea: Origin of a high-velocity layer in the lower crust, Journal of Geophysical Research-Solid Earth, 122, 2831-2858, 10.1002/2016jb013481, 2017.
59. Wang, M., Shang, X., and Duan, T.: A Review of the Establishment Methods of Training Image in Multiple-point Statistics Modeling, Geological Journal of China Universities, 28, 96-103, 2022.
60. Wang, T. K., Chen, M. K., Lee, C. S., and Xia, K.: Seismic imaging of the transitional crust across the northeastern margin of the South China Sea, Tectonophysics, 412, 237-254, 10.1016/j.tecto.2005.10.039, 2006.
61. Wang, X., Hutchinson, D. R., Wu, S., Yang, S., and Guo, Y.: Elevated gas hydrate saturation within silt and silty clay sediments in the Shenhu area, South China Sea, Journal of Geophysical Research-Solid Earth, 116, 10.1029/2010jb007944, 2011.
62. Wang, Q., Zhao, M., Zhang, J., Zhang, H., Sibuet, J.-C., Li, Z., He, E., Qiu, X., Peng, W., and Chen, G.: Breakup mechanism of the northern South China Sea: Evidence from the deep crustal structure across the continent-ocean transition, Gondwana Research, 120, 47-69, 10.1016/j.gr.2022.09.004, 2023.
63. Wei, X., Ruan, A., Zhao, M., Qiu, X., Wu, Z., and Niu, X.: Shear wave velocity structure of Reed Bank, southern continental margin of the South China Sea, Tectonophysics, 644, 151-160, 10.1016/j.tecto.2015.01.006, 2015.
64. Wei, X.-D., Ruan, A.-G., Zhao, M.-H., Qiu, X.-L., Li, J.-B., Zhu, J.-J., Wu, Z.-L., and Ding, W.-W.: A wide-angle OBS profile across Dongsha Uplift and Chaoshan Depression in the mid-northern South China Sea, Chinese Journal of Geophysics-Chinese Edition, 54, 3325-3335, 10.3969/j.issn.0001-5733.2011.12.030, 2011.
65. Wu, S., Zhang, G., Huang, Y., Liang, J., and Wong, H. K.: Gas hydrate occurrence on the continental slope of the northern South China Sea, Marine and Petroleum Geology, 22, 403-412, 10.1016/j.marpetgeo.2004.11.006, 2005.
66. Wu, Z., Li, J., Ruan, A., Lou, H., Ding, W., Niu, X., and Li, X.: Crustal structure of the northwestern sub-basin, South China Sea: Results from a wide-angle seismic experiment, Science China-Earth Sciences, 55, 159-172, 10.1007/s11430-011-4324-9, 2012.
67. Xia, S., Fan, C., Wang, D., Cao, J., and Zhao, F.: Hyperextended crustal structure of the Qiongdongnan Basin and subsequent magmatic influence from the Hainan mantle plume, Science China-Earth Sciences, 65, 845-862, 10.1007/s11430-021-9894-7, 2022.
68. Xia, S., Zhao, F., Zhao, D., Fan, C., Wu, S., Mi, L., Sun, J., Cao, J., and Wan, K.: Crustal plumbing system of post-rift magmatism in the northern margin of South China Sea: New insights from integrated seismology, Tectonophysics, 744,

227-238, 10.1016/j.tecto.2018.07.002, 2018.

69. Xia, S., Zhao, F., Zhao, D., Fan, C., Wu, S., Mi, L., Sun, J., Cao, J., and Wan, K.: Crustal plumbing system of post-rift magmatism in the northern margin of South China Sea: New insights from integrated seismology, Tectonophysics, 744, 227-238, 10.1016/j.tecto.2018.07.002, 2018.
70. Xie, X., Zhao, S., Ren, J., Yang, Y., and Yao, Y.: Marginal Sea Closure Process and Genetic Mechanism of South China Sea during Post-Spreading Period, Earth Science, 47, 3524-3542, 2022.
71. Xiong, C., Cao, J., Sun, J., Xia, S., Wan, K., Fan, C., and Yang, B.: Variation Characteristics along the Strike of the Littoral Fault Zone in Offshore Pearl River Estuary, Earth Science, 43, 3682-3697, 2018.
72. Xu, Z., Hu, T., Pang, X.-Q., Wang, E.-Z., Liu, X.-H., Wu, Z.-Y., Chen, D., Li, C.-R., Zhang, X.-W., and Wang, T.: Research progress and challenges of natural gas hydrate resource evaluation in the South China Sea, Petroleum Science, 19, 13-25, 10.1016/j.petsci.2021.12.007, 2022.
73. Yan, P., Zhou, D., and Liu, Z. S.: A crustal structure profile across the northern continental margin of the South China Sea, Tectonophysics, 338, 1-21, 2001.
74. Yang, L., Hou, W., Cui, C., and Cui, J.: GOSIM: A multi-scale iterative multiple-point statistics algorithm with global optimization, Computers & Geosciences, 89, 57-70, 10.1016/j.cageo.2015.12.020, 2016.
75. Yao, L., Dimitrakopoulos, R., and Gamache, M.: Learning high-order spatial statistics at multiple scales: A kernel-based stochastic simulation algorithm and its implementation, Computers & Geosciences, 149, 10.1016/j.cageo.2021.104702, 2021.
76. Yin, Y., Zhang, C., Li, J., and Shi, S.: Progress and prospect of multiple-point geostatistics, Journal of Palaeogeography, 13, 245-252, 2011.
77. Yu, Z., Li, J., Ding, W., Zhang, J., Ruan, A., and Niu, X.: Crustal structure of the Southwest Subbasin, South China Sea, from wide-angle seismic tomography and seismic reflection imaging, Marine Geophysical Research, 38, 85-104, 10.1007/s11001-016-9284-1, 2017.
78. Yu, S., Li, S., He, Y., Duan, T., Lian, P., Tao, J., and Bao, X.: Multiple-point geostatistics algorithm based on pattern scale-down cluster, Acta Petrolei Sinica, 37, 1403-1409, 2016.
79. Zhang, J., Wu, Q., and Hao, D.: Framework for mine-water inrush scene constructing and drilling trajectory planning: a case study in the Zijiang Coal Mine, China, Arabian Journal of Geosciences, 12, 10.1007/s12517-019-4643-2, 2019.
80. Zhang, T., Switzer, P., and Journel, A.: Filter-based classification of training image patterns for spatial simulation, Mathematical Geology, 38, 63-80, 10.1007/s11004-005-9004-x, 2006.
81. Zhang, J., Li, J., Ruan, A., Wu, Z., Yu, Z., Niu, X., and Ding, W.: The velocity structure of a fossil spreading centre in the Southwest Sub-basin, South China Sea, Geological Journal, 51, 548-561, 10.1002/gj.2778, 2016.
82. Zhang, J., Zhao, M., Sun, Z., Sun, L., Xu, M., Yang, H., Wang, Q., Pang, X., Zheng, J.,

and Yao, Y.: Large volume of magma involved in South China Sea rifting: Implication for mantle breakup earlier than crust, Tectonophysics, 853, 10.1016/j.tecto.2023.229801, 2023.

83. Zhao, M., He, E., Sibuet, J.-C., Sun, L., Qiu, X., Tan, P., and Wang, J.: Postseafloor Spreading Volcanism in the Central East South China Sea and Its Formation Through an Extremely Thin Oceanic Crust, Geochemistry Geophysics Geosystems, 19, 621-641, 10.1002/2017gc007034, 2018.
84. Zhao, M., Yuan, Y., Zhang, C., Gao, J., Su, X., Wang, X., Cheng, J., and Zhang, J.: Deep seismic structure of the continent-ocean transition in the northern margin of the South China Sea revealed by jointly reflective and refractive data along OBS2018-H2 profile, Chinese Journal of Geophysics-Chinese Edition, 65, 2210-2225, 10.6038/cjg2022P0793, 2022.
85. Zhu, J., Xu, H., Qiu, X., Ye, C., and Li, S.: Crustal structure and rifting of the northern South China Sea margin: Evidence from shoreline-crossing seismic investigations, Geological Journal, 53, 2065-2083, 10.1002/gj.3034, 2018.

Appendices

A. Simulated results of the new algorithm compared to other algorithms

In this section, we present a comparison of the multi-source heterogeneous data fusion model (Fig. A1) developed in this study with the model that does not utilize multi-source heterogeneous data (Fig. A2), the Kriging interpolation model (Figure A3), and the MPS interpolation model (Fig. A4).

https://doi.org/10.5194/egusphere-2024-684
Preprint. Discussion started: 26 March 2024

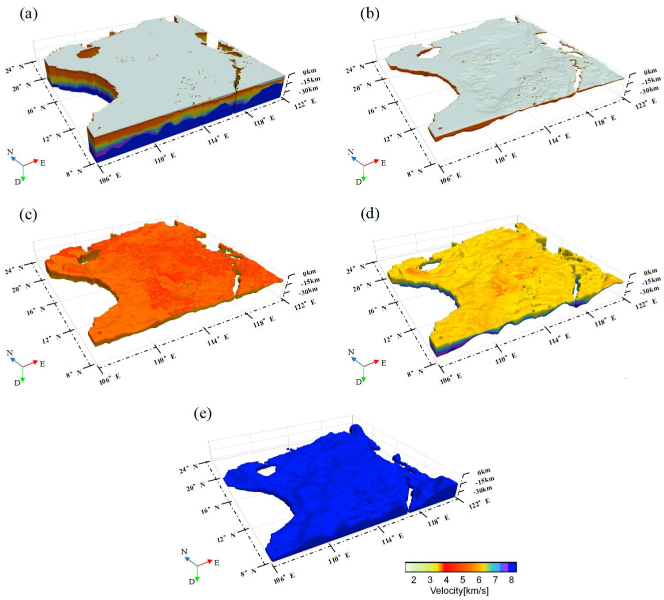

Figure A1 The modeling results of the SCS structure model constructed by integrating multi-source heterogeneous data. (a) is the overall 3D velocity structure model. (b) represents the result of modeling for the sedimentary layer, (e) for the upper crust, and (d) and (e) respectively represent the lower crust and mantle in the modeling results.

https://doi.org/10.5194/egusphere-2024-684
Preprint. Discussion started: 26 March 2024

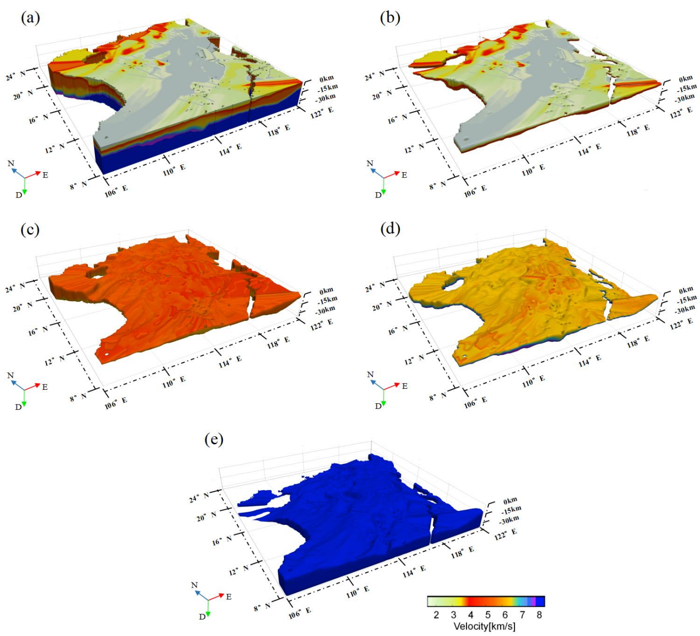

921

922 Figure A2 The modeling results of the SCS model constructed without

923 integrating multi-source heterogeneous data. (a) is the overall 3D velocity structure

924 model. (b) represents the result of modeling for sedimentary layer, (c) for the upper

925 crust, and (d) and (e) respectively represent the lower crust and Mantle in the

926 modeling results.

927

https://doi.org/10.5194/egusphere-2024-684
Preprint. Discussion started: 26 March 2024

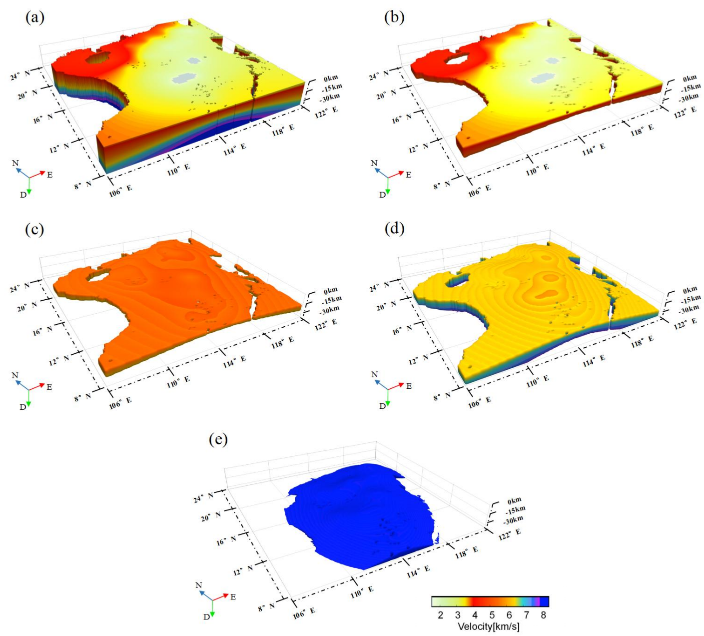

Figure A3 The modeling results of the SCS model constructed by Kriging interpolation. (a) is the overall 3D velocity structure model. (b) represents the result of modeling for the sedimentary layer, (c) for the upper crust, and (d) and (e) respectively represent the lower crust and Mantle in the modeling results.

https://doi.org/10.5194/egusphere-2024-684
Preprint. Discussion started: 26 March 2024

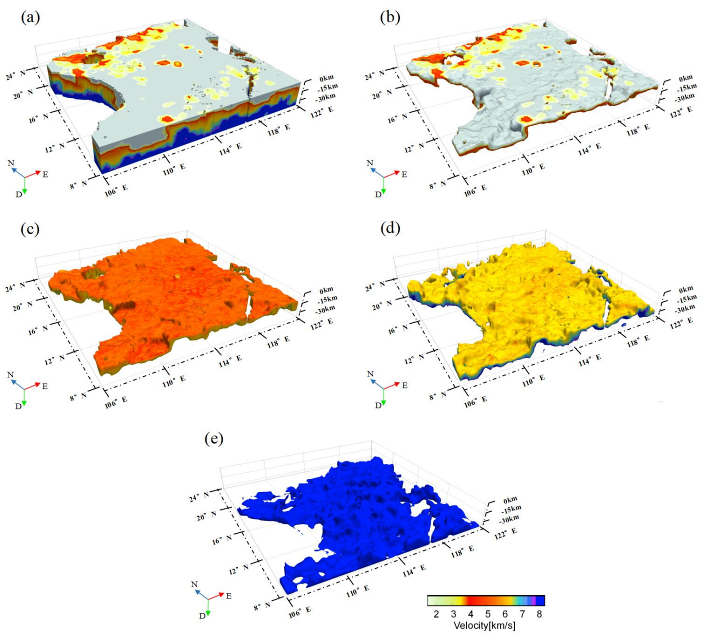

Figure A4 The modeling results of the SCS model constructed by Multipoint statistics. (a) is the overall 3D velocity structure model. (b) represents the result of modeling for the sedimentary layer, (c) for the upper crust, and (d) and (e) respectively represent the lower crust and Mantle in the modeling results.

B. Comparison of profiles with other algorithms

In this section, we present a comparison of the simulation results of each algorithm at the corresponding position profile without adding OBS2012-2 (Fig. B1) and OBS973-2 (Fig B2) to the original data. Together with OBS2017-2, these three profile data are located at the northeast edge, south edge, and central part of the study area, and the amount of data from other OBS profiles around them also varies significantly. In this case, the results of the three profiles are compared, and the models constructed by our new algorithm are closer to the real situation.

https://doi.org/10.5194/egusphere-2024-684
Preprint. Discussion started: 26 March 2024

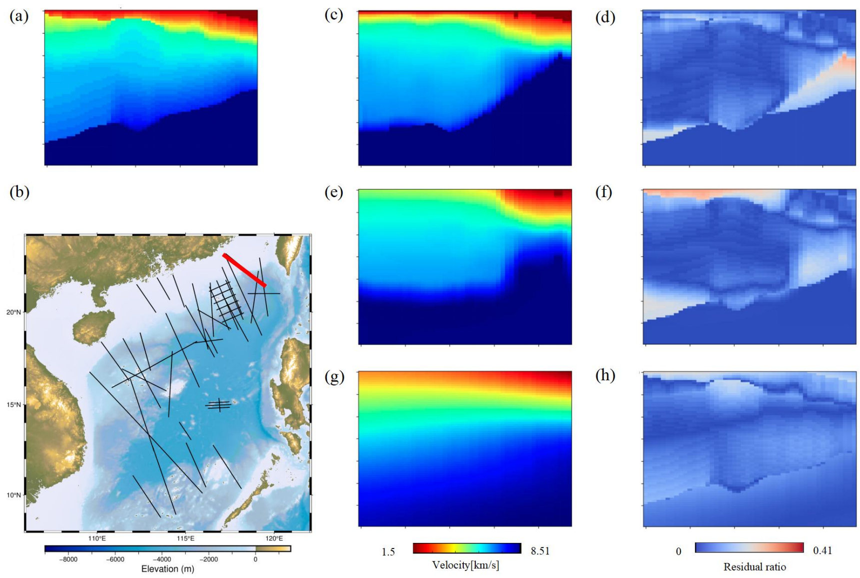

Figure B1 (a) OBS2012-2 forward modeling profile. (b) Schematic diagram of the location of OBS2012-2 profile data, where the red line represents the OBS2012-2 profile.(c) (e) (g) are the profiles of OBS2012-2 position in the model constructed by using multi-source heterogeneous data, not using multi-source heterogeneous data, and Kriging interpolation respectively, and (d) (f) (h) are the residual maps of these profiles and OBS2012-2 profile data.

https://doi.org/10.5194/egusphere-2024-684
Preprint. Discussion started: 26 March 2024

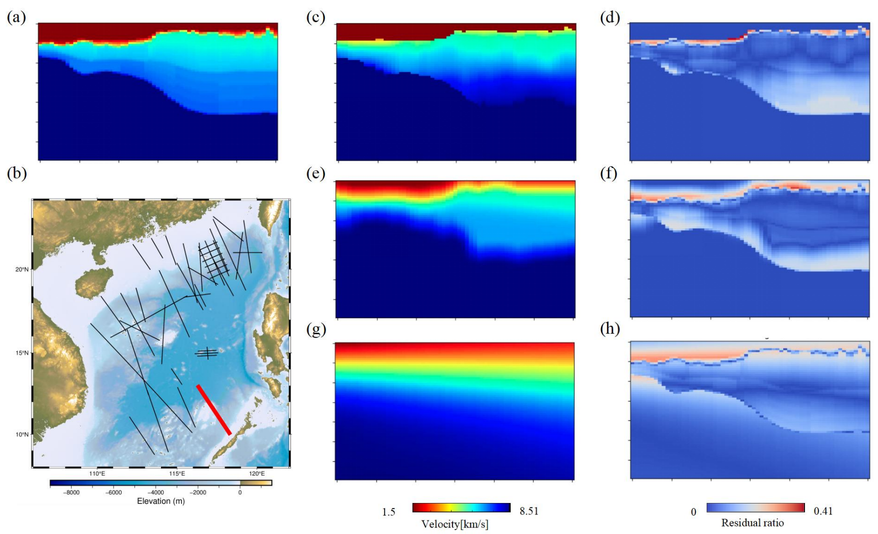

Figure B2 OBS973-2 forward modeling profile. (b) Schematic diagram of the location of OBS973-2 profile data, where the red line represents the OBS973-2 profile.(c) (e) (g) are the profiles of OBS973-2 position in the model constructed by using multi-source heterogeneous data, not using multi-source heterogeneous data, and Kriging interpolation respectively, and (d) (f) (h) are the residual maps of these profiles and OBS973-2 profile data.